ANNUAL REPORT

July 1987

ELECTRONIC HETERODYNE MOIRE DEFLECTOMETRY - A METHOD FOR TRANSIENT AND THREE DIMENSIONAL DENSITY FIELDS MEASUREMENTS

Josef Stricker

Technion, Israel Institute of Technology
Haifa, Israel 32000

RECEIVED BY
NASA STI FACILITY
DATE: 8-7-87
DCAF NO. 016600
PROCESSED BY
☑ NASA STI FACILITY
☐ ESA - SDS ☑ AIAA

Annual Report

ELECTRONIC HETERODYNE MOIRE DEFLECTOMETRY — A METHOD FOR
TRANSIENT AND THREE DIMENSIONAL DENSITY FIELDS MEASUREMENTS*

Josef Stricker

Technion, Israel Institute of Technology
Haifa, Israel 32000

ACKNOWLEDGEMENTS

ABSTRACT

Effects of diffraction and non-linear photographic emulsion characteristics on the performance of deferred electronic heterodyne moire deflectometry are investigated. The deferred deflectometry is used for measurements of non-steady phase objects where it is difficult to complete the analysis of the field in real time. The sensitivity, accuracy and resolution of the system are calculated and it is shown that they are weakly affected by diffraction and by non-linear recording. The features of the system are significantly improved compared with the conventional deferred intensity moire technique, and are comparable with the on-line heterodyne moire. The system was evaluated experimentally by deferred measurements of the refractive index gradients of a weak phase object consisting of a large KD*P crystal. This was done by photographing the phase object through a Ronchi grating and analyzing the transparency with the electronic heterodyne readout system. The results are compared with the measurements performed on the same phase object with on-line heterodyne moire deflectometry and with heterodyne holographic interferometry methods. A good agreement was observed. Some practical considerations for system-improvement are discussed.

In the second part of the project, an algorithm for reconstruction of 3-D phase objects from incomplete deflections data, has been developed. The algorithm is based on the inverse Cormack transformation. The advantages of the present reconstruction method are: 1. The measured deflections are readily used in the inversion transform; no numerical derivations have to be performed like in the case of interferometry. 2. No iterations between the object domain and the projection domain are necessary. The algorithm has been evaluated by a computer simulation; an asymmetric analytical density field around a circular opaque object was successfully reconstructed.

TABLE OF CONTENTS

FIGURE CAPTIONS

Fig. 1. Schematics of a conventional moire system. L.S. is a point light
source (may be a focused laser beam). M is a parabolic mirror. G_1
and G_2 are Ronchi rulings and S is a mat transparent screen.

Fig. 2. Schematic of the setup for recording the phase object. ϕ is the
refraction angle; R(x) is the distance from the phase object at which
the refracted ray seems to emerge.

Fig. 3. Schematic of the experimental setup for postanalyzing phase objects:
G, Ronchi ruling; R.S. and T.S., reference and test signals
respectively; G.S., gating signal.

Fig. 4. Intensity transmittance – exposure curves.
a) For Agfa Gevaert 10E75 plate; the dashed curve is the third-order
polynomial approximation, and b) For Kodak G49F plate; the dashed
curve is the second-order polynomial approximation.
E_L and E_o are respectively the width of the linear portion of the
curves and the exposure at which they start.

Fig. 5. Calculated moire intensity vs. phase for various values of f. f = 0.0,
0.02, 0.04, 0.10, 0.15, 0.20, 0.25, 0.30, 0.35, 0.40, 0.45, and 0.50
for (a), (b), (c), (d), (e), (f), (g), (h), (i), (j), (k), and (l)
respectively. In each figure, the upper two curves are for
Agfa-Gevaert 10E75 plates prefogged with exposure $E_o = 12$ erg/cm^2
and with E' = 8 erg/cm^2 and E' = 18 erg/cm^2 for the solid line and
dashed line, respectively. The lower curve is for Kodak 649F plates
with $E_o = 0$ and E' = 55 μJ/cm^2.

PART 1 PERFORMANCE OF MOIRE DEFLECTOMETRY WITH DEFERRED

ELECTRONIC HETERODYNE READOUT

I. INTRODUCTION

Moire deflectometry is a simple technique for optical testing of phase

objects and specular surfaces, based on the moire effect[1-4]. The method

provides mapping of ray deflections caused either by a phase object or upon

reflection from a surface. From this information the index of refraction

field of the phase object or the quality of the reflecting surface are

obtained. A summary of progress through 1984 is contained in the reviewing

article by Kafri and Glatt[5].

A. Background

A conventional moire deflectometer consists of two identical Ronchi

gratings, a collimated light source and a diffusing screen attached to the

output grating. A schematic description of the system is shown in Fig. 1.

The gratings are shown separated by a distance Δ and their lines are rotated

relative to each other by a small angle θ. When a collimated light beam

passes through the gratings a moire pattern is produced on the screen. The

pattern consists of straight fringes perpendicular to the original grating

lines, separated by a distance of p'[1]

$$p' = \frac{p}{2\sin(\theta/2)} \simeq \frac{p}{\theta} \qquad (1)$$

where p is the pitch of the gratings.

The moire effect for very small grating separation distance can be

explained by pure geometrical optics. However, when grating separation

increases, diffraction introduces undesired effects which limit the

performance of the system[6,7]. To minimize these effects, the distance Δ

between the gratings must be exactly one of the Fourier image planes of the

gratings namely[6,7]

$$\Delta_\ell = \ell \frac{p^2}{\lambda} \qquad\qquad \ell = 1,2,3\ldots \qquad\qquad (2)$$

For these distances, the fringe contrast will be maximum. When

$$\Delta = (\ell + \frac{1}{2}) \frac{p^2}{\lambda} \qquad\qquad (3)$$

the fringes will vanish completely. In Eqs. (2) and (3) λ is the wavelength of the collimated light beam.

If the collimated light is refracted by a phase object before it enters the deflectometer, the original straight parallel moire fringes will be distorted. $\phi_x(r)$, the angle of refraction in the x-direction at a point $r \equiv x,y$, is related to the fringe shift $\delta h_y(r)$ in the y-direction by

$$\phi_x(r) = \frac{\theta\ \delta h_y(r)}{\Delta} = \frac{p\ \delta h_y(r)}{p'\ \Delta} \qquad\qquad (4)$$

By measuring $\delta h_y(r)$, $\phi_x(r)$ can be calculated. In turn, the x component of the index of refraction gradient may be calculated by using the equation[1]

$$\phi_x(r) = \frac{1}{n_f} \int_{z_0}^{z_f} \frac{\partial n(r)}{\partial x}\ dz \qquad\qquad (5)$$

or

$$\phi_x(r) = \frac{G}{n_f} \int_{z_0}^{z_f} \frac{\partial \rho(r)}{\partial x}\ dz \qquad\qquad (6)$$

where z_0 and z_f are the boundaries of the phase object along the line of sight, n is the index of refraction which is related to the density ρ by

$$n - 1 = G \rho \qquad\qquad (7)$$

where the coefficient G is the Gladstone-Dale constant, a function of the wavelength λ. For air, at a wavelength of λ = 6328 Å, G = 0.227 cm^3/gr. n_f is the index of refraction of the medium surrounding the object.

B. Electronic Heterodyne Method

Recently, the accuracy and sensitivity of the moire method, for on-line real time measurements, has been significantly improved by applying the heterodyne technique for reading the deflections of the moire fringes[8-10]. The basic idea of the heterodyne technique is to measure the phase of the signal from a photodetector detecting the light transmitted through a travelling moire fringe pattern. The moving fringes may be accomplished by translating the output grating G_2 relative to G_1 at a constant speed V in the x-direction. When the collimated light is not disturbed by the phase object (straight line fringes), the first harmonic of the photodetector signal is given by[9]

$$I(y,\Delta^*,t) = \frac{2}{\pi^2}\cos(\pi\Delta^*)\cos[2\pi(\frac{x}{p} + \frac{y\theta}{p} + \frac{\Omega}{2\pi}t)] \qquad (8)$$

where $\Delta^* = \Delta/(p^2/\lambda)$ is the distance between the gratings in Fourier units and x/p and $y\theta/p$ are phase shifts related to the relative translation and rotation of the Ronchi gratings. Here x is the x-directed offset between the lines of the two gratings. Ω is the fundamental frequency

$$\Omega = 2\pi\frac{V}{p} \qquad (9)$$

In deriving Eq. 8 the following assumptions were made:
1. Paraxial approximation.
2. Slow variations of the phase object over a pitch scale.
3. Small θ.
4. Fresnel diffraction.

The effect of refraction by a phase object is to introduce a phase shift[9]

$$\Delta\psi(r) = 2\pi \frac{\phi_x(r)\Delta}{p} \tag{10}$$

A procedure for measuring this phase shift is to record the electronic phase relative to that of a reference signal, with and without the phase object, and subtracting the two phases. Equations (4) and (6) are then used to compute the properties of the phase object. Since phase measurements can be accomplished for better than a degree, fringe interpolation accuracies better than 1/360 fringe are possible.

C. Transient Phase Objects

When unsteady phenomena occur, it is difficult to complete the analysis of the whole field in real time. In these cases, it is necessary to freeze the phase object and post-analyze it after the fact[11,12]. The idea of applying the electronic heterodyne readout technique for the deferred moire fringes readout was recently demonstrated[13]. In this case, the second Ronchi grating (see Fig. 2) is replaced by a photographic plate. The phase object is recorded on the photographic plate by exposing it to the collimated beam transmitted through the phase object and the first grating, thus the distorted image of the first grating due to refraction by the phase object is recorded. Readout is accomplished by placing the moving grating immediately in back of the processed photographic plate as shown in Fig. 3. When the combination is illuminated, a time varying signal is obtained and analyzed by the heterodyne technique in a manner similar to that described for the on-line case.

The purpose of this work is to investigate, both analytically and experimentally, the effects of diffraction and non-linear response of the photographic film on the performance of the deferred heterodyne moire

deflectometry. The resolution, accuracy, and sensitivity of the method will be evaluated and compared with those of the real-time moire deflection method. Some practical considerations for the most efficient use of this method will be discussed.

In the next section, the theory of the method is presented and in Sec. III mapping the index of refraction of a weak phase object using this method is demonstrated.

II. THEORY

As mentioned above the measurements of the density field of a transient phase object involves three steps: Recording, moire fringe formation, and electronic heterodyne readout. First, the distorted shadow of the first grating is recorded on a photographic plate when placed in the position of the second grating - Fig. 2. The grating is illuminated with the collimated beam passing through the phase object. The photographic plate is later processed to a transparency, which later is referred to as the phase object transparency. The distortion of the grooves of G are mainly caused by three reasons:

1. Refraction by the phase object.

2. Diffraction by the Ronchi grid.

3. Non-linear response of the photographic emulsion.

This step is repeated when the phase object is absent, the transparency obtained is called the reference transparency. Even in this case the image of the grooves may be distorted as a result of diffraction and non-linear photographic effects.

Next, the moire fringes are formed by placing the shadow transparency in front of the second Ronchi grating. When the combination is illuminated, moire fringes are observed. Since the shadow transparency and the Ronchi grating are in contact, the formation of moire fringes is a purely geometrical effect.

The readout step is accomplished by translating the grating (thus causing the moire fringes to move) and recording the phase of the signal output of the photodetector (Fig. 3) as described for the on-line case.

In the course of calculating the output signal of the photodetector we will follow the three steps described above.

A. Intensity Transmission Distribution of the Transparency

Assuming an infinite Ronchi grating with square wave line profile illuminated by an infinite beam, and assuming Fresnel diffraction, the intensity distribution of the beam passing through the phase object and the Ronchi grating at a distance Δ (where the photographic plate is located) is given by[7]:

$$I(u,\Delta^*,\xi) = u\left\{\frac{1}{4} + \frac{2}{\pi} \sum_{n=0}^{\infty} \frac{\sin[2\pi(2n+1)u\xi]}{(2n+1)} \cos[\pi(2n+1)^2 u\Delta^*] + \right.$$

$$+ \frac{4}{\pi^2} \sum_{n=0}^{\infty} \frac{\sin^2[2\pi(2n+1)u\xi]}{(2n+1)^2} + \frac{8}{\pi^2} \sum_{n\neq m} \frac{\sin[2\pi(2n+1)u\xi]}{(2n+1)} \times$$

$$\left. \times \frac{\sin[2\pi(2m+1)u\xi]}{(2m+1)} \cos\{\pi u\Delta^*[(2n+1)^2 - (2m+1)^2]\}\right\} \tag{11}$$

where $\xi = x/p$, $u = \frac{R(x)}{\Delta + R(x)}$ and $R(x)$ and $\phi_x(r)$ are defined in Fig. 1. In deriving Eq. (11) the paraxial approximation was assumed, which in this case means that $R(x) \gg \Delta, x$. According to this assumption it is clear that the intensity in Eq. (11) is practically independent on the origin of coordinates. Note that when no phase object exists, $u = 1$. The transmittance of the photographic plate is proportional to this spatially varying intensity.

Generally it is assumed that there is a linear relation between $|T|^2$, the intensity transmittance of the photographic plate, and the exposure E. However, the actual $|T|^2$-E curves for photographic materials are always

nonlinear to some degree. Figures 4a and 4b display the $|T|^2$-E curves for a Agfa-Gevaert 10E75 plate and for a 649F Kodak plate, respectively. In the figure, E_0 denotes the exposure at which the linear region starts and E_L denotes the width of the linear portion of the curve.

If the photographic plate is uniformly prefogged by exposure E_0, and illuminated by a pattern of amplitude E' (the total exposure is E_0 + E') then a moderate portion of the $|T|^2$-E curve can be approximated by a cubic polynomial,

$$|T|^2 = R_0 + R_1(E_0 + E') + R_2(E_0 + E')^2 + R_3(E_0 + E')^3 \tag{12}$$

Figure 4a illustrates the polynomial approximation for the Agfa-Gevaert plate with E_0 = 12 erg/cm^2, $0 \le E' \le 18$ erg/cm^2, R_0 = 1.1847, R_1 = -7.4385 x 10^{-2} R_2 = 1.5550 x 10^{-3}, and R_3 = -1.0726 x 10^{-5}. In this exposure range, the third order term is small and may be neglected. The dashed curve in Fig. 4b is a quadrature polynomial approximation for the Kodak plate; here E_0 = 0, $0 \le E' \le 53$ µJ/cm^2, R_0 = 8.6668 x 10^{-1}, R_1 = -5.3625 x 10^{-3}, and R_2 = - 7.3440 x 10^{-5}. Replacing E' in Eq. 12 by I, given in Eq. 11, times the intensity of the collimated light beam used for illumination, $|T|^2$ may be written as

$$|T|^2 = a_0 + a_1 I + a_2 I^2 \tag{13}$$

where the coefficients a_0, a_1, and a_2 include all the parameters which appear in Eq. 12 and the intensity of the light beam used for the illumination.

B. The Moire Image

The moire image is evaluated by multiplying the intensity transmittance distribution of the transparency and that of the grating, and averaging the

product over a pitch distance, namely[6]

$$M(r,\Delta,R,\phi) = \int_{\xi}^{\xi+1} |T|^2 G \, d\xi \qquad (14)$$

where $|T|^2$ is given in Eq. 13 and G, the intensity transmittance distribution of the grid is represented by a Fourier series[7]

$$G(\xi,y) = \frac{1}{2} + \frac{2}{\pi} \sum_{n=0}^{\infty} \frac{\sin[2\pi(2n+1)(\xi+\chi/p+y\theta/p)]}{2n+1} \qquad (15)$$

where χ/p and $y\theta/p$ represent the phase shifts related to the relative translation and rotation of the Ronchi grating. G is not affected by diffraction since the light intensity is measured directly behind the grating.

When Eqs. (11), (13) and (15) are substituted in Eq. (14) and the integration is performed, we get:

$$M(r,\Delta,R,\phi_x) = A + B \sum_{n=0}^{\infty} \frac{\cos^2[\pi u \Delta^*(2n+1)^2]}{(2n+1)^2} +$$

$$+ C \sum_{m,n,k,\ell=0}^{\infty} \frac{\cos\{\pi u \Delta^*[(2n+1)^2-(2m+1)^2]\}}{(2n+1)(2m+1)} \frac{\cos\{\pi u \Delta^*[(2k+1)^2-(2\ell+1)^2]\}}{(2k+1)(2\ell+1)} \delta(m,n,k,\ell)$$

$$+ D \sum_{n=0}^{\infty} \frac{\cos[2\pi(2n+1)(\frac{\chi}{p}+\frac{y\theta}{p}+\frac{\phi_x\Delta}{p})]}{(2n+1)^2} \cos[\pi u \Delta^*(2n+1)^2]$$

$$(16)$$

$$+ E \sum_{m,n,k,\ell=0}^{\infty} \frac{\cos[2\pi(2n+1)(\frac{\chi}{p}+\frac{y\theta}{p}+\frac{\phi_x\Delta}{p})]}{(2n+1)} \frac{\cos[\pi u \Delta^*(2m+1)^2]}{(2m+1)} \times$$

$$\times \frac{\cos\{\pi u \Delta^*[(2k+1)^2-(2\ell+1)^2]\}}{(2k+1)(2\ell+1)} \delta(m,n,k,\ell)$$

where $A = \frac{a_0}{2} + \frac{a_1 u}{4} - \frac{3a_2 u^2}{32}$, $B = \frac{a_2 u^2}{\pi^2}$, $C = \frac{B}{2}$, $D = \frac{2a_1 u}{\pi^2} + \frac{a_2 u^2}{\pi^2}$, $E = \frac{4a_2 u^2}{\pi^4}$, and
$\delta(m,n,k,\ell) = \delta[(n-m)-(k-\ell)] + \delta[(n-m)-(\ell-k)] + \delta[(n+m)-(\ell+k)] - \delta[(n-m)-(k+\ell+1)]$
$- \delta[(m-n)-(k+\ell+1)] - \delta[(n+m)-(k-\ell-1)] - \delta[(n+m)-(\ell-k-1)]$, where each δ on the

right hand side of the equation is the Kronecker δ.

As seen from Eq. 16, the moire image is strongly affected by diffraction (associated with the first Ronchi grating) and by nonlinear recording. Since the conventional deferred deflectometry suggests analyzing the moire pattern by measuring the transmitted intensity[11,12], it is interesting to display the moire image as calculated in Eq. 16. Figures 5a-5l illustrate the moire intensity vs the phase ($x/p+y\theta/p$), for various grating-photographic plate distances. All curves shown are without a phase object i.e. $u = 1$ and $\phi_x = 0$. The distances are $\Delta = \Delta_\ell + f\Delta_1$ where f is a fraction that was varied in the range of 0.00-0.50. Δ_ℓ and Δ_1 are defined in Eq. 2. In each figure the two upper curves are the results for Agfa-Gevaert plates, prefogged with $E_0 = 12$ erg/cm^2 and exposed, through the grating, by a collimated beam with $E' = 8$ erg/cm^2 and $E' = 18$ erg/cm^2 for the solid and dashed curves, respectively. The lower solid curves are for Kodak plates with $E_0 = 0$ and $E' = 55$ μJ/cm^2. Exposure of $E' = 8$ erg/cm^2 falls in the linear region of the Agfa-Gevaert $|T|^2 - E$ curve, thus the $E' = 8$ erg/cm^2 moire intensity curves exhibit only effects of diffraction. The effects of nonlinear recording may be observed by comparing the $E' = 8$ erg/cm^2 curves with the $E' = 18$ erg/cm^2 and with the $E' = 55$ μJ/cm^2 curves which are affected both by diffraction and nonlinear recording.

For $f = 0$ a triangular wave form is obtained, both for the linear and nonlinear curves (Fig. 5a). At this distance, the exact dependence of the moire image on the phase is known, thus neither diffraction nor nonlinearity affect the accuracy and sensitivity of the system[7]. As f increases, the behaviour is changed: the maxima and minima are rounded, the contrast is reduced and higher spatial frequency waves are superimposed on the triangular wave. These changes are more pronounced in the nonlinear curves, and thus may

introduce higher uncertainties in the deflection measurements. At f = 0.25 the wave form is again triangular, but with lower contrast as compared to that of f = 0. At f = 0.50 the intensity is independent of the phase and the contrast is zero. These results are of practical importance since experimentally it is hard to adjust the spacing between the Ronchi grating and the photographic plate to be exactly one of the Fourier image planes, especially in the case of an arbitrary phase object where such a single spacing, for the whole object, does not exist[6,7].

C. Heterodyne Readout

As in the case of the on-line heterodyne moire, the heterodyne readout is accomplished by translating the Ronchi grating relative to the photographic transparency in the x-direction. The motion will cause the moire fringes to move in the y-direction. Assuming a linear motion of the grating with speed V, the phase of the moire image will vary with time as

$$\psi(y,t) = 2\pi(\frac{X}{p} + \frac{y\theta}{p} + \frac{\phi_x\Delta}{p} + \frac{\Omega}{2\pi} t) \tag{17}$$

where $\Omega = 2\pi \frac{V}{p}$. If the higher harmonics of the signal given by Eq. 16 are filtered out, the signal is given by:

$$M_{T1}(r,R,\Delta,t,\phi_x) = \cos[2\pi(\frac{X}{p} + \frac{y\theta}{p} + \frac{\phi_x\Delta}{p} + \frac{\Omega}{2\pi} t)] \{D\cos(\pi u\Delta^*) +$$

$$+ E \sum_{m,k,\ell=0}^{\infty} \frac{\cos[\pi u\Delta^*(2m+1)^2]}{2m+1} \frac{\cos\{\pi u\Delta^*[(2k+1)^2-(2\ell+1)^2]\}}{(2k+1)(2\ell+1)} \delta(m,n=0,k,\ell)\} \tag{18}$$

The fundamental frequency component of Eq. (16), for the reference transparency is:

$$M_{R1}(y,\Delta^*,t) = \cos[2\pi(\frac{x}{p} + \frac{y\theta}{p} + \frac{\Omega}{2\pi}\ t)]\{D\cos(\pi\Delta^*) +$$

$$+ E\ \sum_{m,k,\ell=0}^{\infty}\ \frac{\cos[\pi\Delta^*(2m+1)^2]}{2m+1}\ \frac{\cos\{\pi\Delta^*[(2k+1)^2-(2\ell+1)^2]\}}{(2k+1)(2\ell+1)}\ \delta(m,n=o,k,\ell)\}$$

(19)

Comparing the transmitted signals with and without the phase object, it is seen that the effect of refraction is to introduce a phase shift $\Delta\psi(r)$ given by

$$\Delta\psi(r) = 2\pi\ \frac{\phi_x(r)\Delta}{p}$$

(20)

already discussed in connection with Eq. 10. The procedure for measuring this phase shift is similar to that described for the on-line heterodyne deflectometry[9,10]. The phase of the signal, relative to a reference signal is measured twice at each point on the combination transparency-grating: once with the transparency recorded with the phase object and once with the transparency recorded without the phase object. The difference between the two readings gives the absolute phase shift given by Eq. 20. The reference signal is the output of a photodetector placed at a fixed point in part of the fringe pattern not affected by the phase object.

D. Advantages of the Heterodyne Readout

The theoretical analysis above shows some of the advantages of the deferred electronic heterodyne readout technique over the conventional deferred intensity readout method:

1. The errors introduced because of inaccurate positioning of the photographic plate precisely on one of the Fourier planes (diffraction and the nonlinear recording effects) are small compared with those in intensity measurements. This is true since the electronic phase recording

of the fundamental frequency signal is insensitive to small fringe contrast variations and to the fine structure of the fringes (see Fig. 5).

2. Variations of intensity over the fringe pattern due to optical imperfections and other effects do not affect the phase measurements since the phase is computed as a quotient of two intensity terms[9]. However, for intensity measurements, this effect may lead to significant errors.

3. The electronic heterodyne method has the ability to interpolate continuously between fringe maxima, and has computer compatibility.

4. In principle, by using the third harmonic term of Eq. 16 (with the time varying phase term $3 \frac{\Omega}{2\pi} t$) the electronic phase of $3\Delta\psi$ will be measured, which is equivalent to tripling the sensitivity of the system[9].

E. Spatial and Angular Resolution

Diffraction effects, detector aperture and electronic instrumentation determine the spatial and angular resolution of the system. Since the nonlinear photographic recordings do not affect the resolution of the system, the results of the spatial and angular resolution obtained for the on-line deflectometry are valid for the present deferred case[9].

The spatial resolution of the system is

$$\frac{\Delta x}{p} = \rho^* + 2\Delta^* \tag{21}$$

where $\rho^* = \rho/p$ is the dimensionless size of the detector.

The angular resolution is given by:

$$(\Delta\theta)_{min} = \frac{\lambda^*}{360 \Delta^*} \tag{22}$$

where $\lambda^* = \lambda/p$.

F. Some Practical Considerations

It is important to point out that the final accuracy and sensitivity of measuring phase $\Delta\psi$ is strongly dependent on the manner in which it is practically performed.

1. The electronic processing of the photographic transparencies is performed on a separate bench. The procedure for measuring $\Delta\psi$ (Eq. 20) is to record the electronic phase, relative to that of a reference signal twice: once when the phase object transparency is placed in front of the grating and once with the reference transparency in front of the grating. $\Delta\psi$ is then obtained by subtraction of the readings. It is clear that the accuracy of the system and the ability to measure small deflections is dependent on the capability to accurately place the two transparencies precisely in the same position relative to the grating and to the detectors. Small misalignments will result in considerable errors in the measured phases and thus in fringe deflections.

2. Practically the phase meter output is dependent on the visibility of the fringes and on the distortions of the fringe profile caused by the nonlinear recording. Increasing the visibility, on the one hand, reduces the error of phase reading. On the other hand it increases the effects of nonlinear recording which affects the measurement as well. Thus in forming the transparencies, one must compromise between those two effects.

In the previous section it was mentioned that by using the third harmonic component of the moire signal, it is possible to tripple the sensitivity of the system. It is worthwhile to point out that practically it is hard to materialize this useful feature since the third harmonic signal is weak and thus the signal-to-noise ratio is low.

III. EXPERIMENTAL

The deferred electronic heterodyne technique was evaluated by measuring small fringe shifts caused by a weak phase object. The phase object used was a large crystal of KD*P whose refractive index distribution could be changed when voltages are applied to the electrodes mounted on the crystal. A detailed description of this phase object, a so-called gas-flow simulator, is given in Ref. 15. The flow simulator was chosen to be tested because of two reasons: a. The flow simulator was previously investigated by the electronic heterodyne holographic interferometry and by the on-line electronic heterodyne moire deflectometry methods[9,10]. The availability of these measurements, which serve as a comparison makes it possible to evaluate the system. b. The flow simulator is a very weak phase object which exhibits a fine structure close to the limit of the angular and spatial resolution of the system. The ability to measure such a phase object validates the theoretical predicted performance.

The moire setup for recording the phase object was the same as that described previously for the on-line experiment[9] except that the second grating was replaced by a photographic plate. We used Agfa-Gevaert 10E75 plates. The phase object transparency was recorded when the high voltage of 5 kv was applied to the crystal. The reference recording was performed with the crystal in place, but without the voltage.

Other parameters in the experiment were the same as those in Ref. 9, namely: the separation between the grating and the photographic plate was $\Delta = 32$ cm, the grating pitch was $p = 0.17$ mm thus $\lambda^* = 3.27 \times 10^{-3}$, $\Delta^* = 7$, the spatial resolution, calculated from Eq. 21 was $\Delta x = 3.1$ mm and the angular resolution, from Eq. 22 was $\Delta \phi_{min} = 1.5 \times 10^{-6}$ rad.

The electronic processing of the developed photographic plates was performed on a separate bench. The distorted moire fringes were observed when

the phase object transparency was placed in front of the Ronchi grating and illuminated by the collimated beam. The separation between the fringes, in the region away from the phase object measured p' = 4.47 mm. The measurement was as follows: while the grating was in motion and the reference detector was fixed at one position, the test detector was moved in the y-direction until the phase meter output covered exactly 360° indicating that the detector had moved a distance equal to p', the period of the moire fringes.

The fringe motion was achieved by engaging the grating, as described in Ref. 10, to an electrical vibrator. The detectors and the rest of the electronic system were the same as those described in Ref. 10. The phases relative to the reference detector, were recorded by a the test detector along the center line of the crystal's image, at stations separated by 1 mm.

At this point the phase object transparency was replaced by the reference transparency and phases were recorded exactly at the same stations as before. The exact positions of the detector were determined by an interferometer. A point by point subtraction of the phases, with and without the phase object, yield the phase shift as a function of position and thus the index of refraction gradient vs. position. The results are shown in Fig. 6a. The results show that the measurements were performed close to the angular and spatial resolution limits. Indices of refraction of the order 2×10^{-6} cm^{-1} were measured and the peak structure of spatial scale of 3-7 mm was resolved.

Figure 6b displays the results measured with the on-line heterodyne deflectometry method. The results obtained with the heterodyne holographic interferometry method are shown for comparison in Fig. 7. The figures show that within the error limits, the results obtained by the three methods agree very well. It is seen that the deferred results are consistently higher, except at the top of the third peak, than those obtained by the two other

methods. The source of this error may result from the transparency misalignment which could have caused a constant phase shift over the whole field.

Reproducibility of the measurements was then tested on a few photographic plates taken of the same object with different exposure levels. We found that the phase $\Delta\psi$ was only reproducible to within $\pm 4°$ over the field. These errors may be attributed to mechanical misalignment of the plates and to contrast variations and non-linear recording effects. More experimental work has to be performed in order to investigate these effects.

For sinusoidal grating motion, rather than motion at a constant velocity, the output of the electronic phase meter does not vary linearly with refraction angle, thus calibration of the system is required[9]. In the present experiment the calibration procedure was the same as that followed in the on-line experiment, except that it was performed with the reference transparency in place (Fig. 3) rather than with the actual KD*P crystral. Similar calibration curves to those shown in Fig. 7 of Ref. 9 were obtained.

Since the accuracy and sensitivity of the system is largely dependent on the transparencies alignment, a special effort was made to put the reference transparency precisely in the same position, relative to the Ronchi grating and to the detection system, as that of the phase object transparency. This was achieved by the following: a. The transparencies were mounted on a plate holder, fixed to the optical bench. The use of the plate holder ensures that the surface coordinates of both transparencies was the same. b. The rotation angle between the reference transparency and the grating was adjusted by measuring p', the separation distance between the moire fringes. The angle was varied until the value of p' reached the same value as that measured with the phase object transparency, namely p'=4.47 mm. c. A geometrical point, photographed on both transparencies, was chosen as a reference point for the

alignment procedure. Before removing the phase object transparency, the x, y coordinates of this point were measured. In order to align the transversal position of the reference grating, it was transversally moved until the x, y coordinates of the reference point attained equal values to those measured on the phase object transparency.

IV. CONCLUSIONS

It has been shown that the electronic heterodyne technique can be applied for accurate and sensitive readout of moire fringes of unsteady phase objects. Theoretically it was shown that the accuracy and sensitivity of the system are weakly affected by diffraction and non-linear photographic emulsion characteristics. The analysis showed that non-linear recording does not affect the spatial resolution of the system. The spatial resolution is mainly affected by diffraction.

The system was evaluated experimentally by mapping a weak phase object. The results compared favorably with observations performed with the electronic heterodyne holographic interferometry and with the on-line heterodyne moire. The theoretical analysis and the experimental measurements have shown that the performance of the the heterodyne deferred moire is of the same order as the on-line heterodyne moire.

The method offers many advantages: low stability requirements, adjustable sensitivity, not affected by noise sources, low cost and computer compatibility. To conclude it can be said that the method is suitable and attractive to use for non-steady phase objects.

The deferred electronic heterodyne moire requires continuing research and development. More experimental investigation is necessary in order to better understand the reasons for the low reproducibility observed. It is suggested

to consistently study the effects of photographic plates exposure levels and developing processes on the system performance. In the present research the only photographic emulsion used was the Agfa-Gevaert 10E75 one, not necessarily the most suitable for moire. Other emulsions with different characteristics should be tested as well. The errors caused by mechanical misalignment of the reference transparency when placed in the position of the phase object transparency, have to be reduced. This can be achieved by including better alignment facilities on the processing bench. Also, as in the on-line case, the sinusoidal motion of the Ronchi grating is undesirable because of the need for calibration. A technique for linear motion has to be developed.

PART 2: MEASUREMENTS OF 3-D DENSITY FIELDS WITH OPAQUE OBJECTS

BY MOIRE DEFLECTOMETRY

I. INTRODUCTION

Tomographic reconstruction of 3-D refractive-index fields from measured

ray deflections by moire method was demonstrated in Ref. 16. It was shown

that if the data on deflections is complete i.e. the field is not blocked by

an opaque object and deflections of 360° coverage are available, the inverse

Radon transform[17,18] may readily be used for field reconstruction. The

advantage of the deflectometry method is that the measured deflections are

directly used in the inversion transformation. This is not the case with

interferometry. Interferometric measurements, namely $\int n dx$ where n is the

index of refraction and x is the distance coordinate along the ray, should be

mathematically processed in order to obtain numerical derivatives. This

process may add errors to the reconstructed field.

In some cases it is desired to use moire deflectometry for measuring 3-D

density fields where an opaque object is present in the field. This situation

occurs when deflectometry is used to study density fields in compressible gas

flowing around a test object or to study the temperature fields around heated

opaque objects, etc. In such cases the object blocks many of the optical rays

used for the measurements and thus part of the data is missing. Since the

missing data is necessary for evaluating the inverse Radon transform, the

direct use of the reconstruction technique is impossible.

The same problem arises when interferometric incomplete data is used for

field reconstruction; Zien et al.[19], Vest and Prikryl[20] and Medoff et

al.[21] proposed to solve the problem by using algorithms based on iterations.

For reconstruction it is necessary to extrapolate the projection data into the

region of missing data. The artificial field evolves during the iterative process by transforming repeatedly between the image domain and the projection domain, applying measured information and other criterions at each iteration. Empirical studies of this algorithm shows[20] that the algorithm does not converge. The studies indicate that the field reaches a best estimate after a number of iterations and then diverges. A similar iteration technique was previously used with deflections data to reconstruct the flow field around a cone at an angle of attack[22]. The problem of algorithm divergence was also encountered in that study.

In many practical situations the opaque object presented in the field is of circular or elliptical cross-section. This occurs in aerodynamics of circular bodies, like cones, at an angle of attack, or in heat-transfer of circular pipes, etc. For such bodies it is shown, that by using the inverse Cormack transform[18,23] the field can be reconstructed directly without the need for iterations. The Cormack transform is based on circular harmonic decomposition of both the image space and the projection space and solving the relation between these decompositions. It is interesting to note that Cormack transform is an extension of Abel transform (for circular symmetric fields Cormack transform reduces to Abel transform).

A brief description of the inverse Cormack transform is given in Sec. II. It is shown how this transform is used with deflections data. An algorithm, based on Cormack transform, is developed and evaluated in Sec. III. The Appendix contains listing of the computer program.

II. THEORY

Cormack's approach is based on the fact that for each r the object function $f(r,\theta)$ is periodic in θ with period 2π, where r and θ are the polar coordinates defined in Fig. 8. Therefore, $f(r,\theta)$ can be expanded in Fourier

Series of the form of

$$f(r,\theta) = \sum_{\ell=-\infty}^{\infty} f_\ell(r)e^{i\ell\theta} \tag{1}$$

where

$$f_\ell(r) = \frac{1}{2\pi} \int_0^{2\pi} f(r,\theta)e^{-i\ell\theta}d\theta \quad . \tag{2}$$

Similarly, the interferometric projection $\lambda(p,\phi)$ can be expanded as

$$\lambda(p,\phi) = \sum_{\ell=-\infty}^{\infty} \lambda_\ell(p)e^{i\ell\phi} \tag{3}$$

with

$$\lambda_\ell(p) = \frac{1}{2\pi} \int_0^{2\pi} \lambda(p,\phi)e^{-i\ell\phi}d\phi \quad . \tag{4}$$

$\lambda(p,\phi)$ is defined by the line integral

$$\lambda(p,\phi) = \int_0^\infty \int_0^{2\pi} f(r,\theta)\delta[p-r\cos(\theta-\phi)]rdrd\theta \tag{5}$$

where the integration is performed over the infinite plane but the delta function in this equation has the effect of reducing the area integral to a line integral along $p=r\cos(\theta-\phi)$, shown in Fig. 8. ϕ is the direction of integration and p is the distance of the line of integration from the origin.

Cormack transform gives the relationship between the Fourier coefficients $\lambda_\ell(p)$ and $f_\ell(r)$[18]:

$$\lambda_\ell(p) = 2 \int_p^\infty \frac{f_\ell(r)\ T_\ell(\frac{p}{r})}{\sqrt{r^2-p^2}} rdr \tag{6}$$

where $T_\ell(\frac{p}{r})$ is the Tschebycheff polynomial of the first kind of order ℓ defined by:

$$T_\ell(x) = \begin{cases} \cos(\ell\cos^{-1}x) & |x| < 1 \\ \cosh(\ell\cosh^{-1}x) & |x| > 1 \end{cases} \tag{7}$$

Note that if $f(r,\theta)$ is rotational symmetric, $f_\ell(r)$ is non-zero only for $\ell=0$ and in this case Eq. 6 reduces to the Abel transform, since $T_0(x)=1$ for all x.

For the reconstruction of the object from its projections, we must determine the inverse Cormack transform i.e. to express $f_\ell(r)$ explicitly. The solution, in one of its forms, is given by[18]:

$$f_\ell(r) = -\frac{1}{\pi} \int_r^\infty \frac{\frac{d\lambda_\ell(p)}{dp} T_\ell(\frac{p}{r})}{\sqrt{p^2-r^2}} \, dp \tag{8}$$

Interesting features of this result are:

1. Only values of $\lambda(p,\phi)$ for $p>r$ are required to reconstruct $f(r,\theta)$, thus Eq. 8 can directly be used for reconstructing fields around circular objects since the data gap in the region $p<r$ is not required for the integration.

2. The derivatives $\frac{d\lambda_\ell(p)}{dp}$, which appear in Eq. 8, are exactly the ℓ'th Fourier coefficients of the function $\frac{\partial\lambda(p,\phi)}{\partial p} \equiv \lambda'(p,\phi)$. The proof is straightforward, since $\lambda(p,\phi)$ is periodic in ϕ, $\lambda'(p,\phi)$ is also periodic, therefore can be expanded in Fourier series of the form of:

$$\lambda'(p,\phi) = \sum_{\ell=-\infty}^{\infty} \lambda_\ell^*(p)e^{i\ell\phi} \tag{9}$$

where

$$\lambda_\ell^*(p) = \frac{1}{2\pi} \int_0^{2\pi} \lambda'(p,\phi)e^{-i\ell\phi}d\phi \tag{10}$$

by applying Eq. 4, Eq. 10 may be written as

$$\lambda_\ell^*(p) = \frac{1}{2\pi} \frac{\partial}{\partial p} \int_0^{2\pi} \lambda(p,\phi)e^{-i\ell\phi}d\phi = \frac{d\lambda_\ell(p)}{dp} \tag{11}$$

It turns out that $\frac{\partial\lambda(p,\phi)}{\partial p}$ is measured directly by deflectometry[1] and therefore no differentiation of experimental data is required prior to the expansion of the measured data in Fourier series.

III. COMPUTER SIMULATION

The reconstruction procedure discussed in the preceding section was evaluated by a computer simulation. The phase object studied was analytically defined and the algorithm was used to reconstruct the object from computed-generated deflections data. The object function was zero everywhere outside a circle of radius R_0, and an opaque object of circular cross section of radius R_c was placed in the object field. In order to have a basis for comparison of the accuracy of the reconstruction obtained in the present work with that obtained by using an iteractive method, we chose to study the same object as that studied by Vest in Ref. 20.

The phase object studied, shown in Fig. 9 is given by:

$$f(x,y) = \exp\left\{\frac{-6[(x-0.6)^2+y^2]}{1-(x^2+y^2)}\right\} + 0.5 \exp\left\{\frac{-6[(x+0.6)^2+y^2]}{1-(x^2+y^2)}\right\}$$

$$+ \exp\left\{\frac{-6[x^2+(y-0.6)^2]}{1-(x^2+y^2)}\right\} + 0.5 \exp\left\{\frac{-6[x^2+(y+0.6)^2]}{1-(x^2+y^2)}\right\} \tag{12}$$

for $\quad R_c \leq r < R_0$

and $\quad f(x,y) = 0 \quad$ for $\quad 0 \leq r < R_c \quad$ and $r \geq R_0$.

The computer simulation program, listed in the Appendix, consists of the following steps:

1. Numerical generation of deflections data, $\lambda'(p,\phi)$. For this purpose $f(x,y)$ was expressed as a function of p, s, and ϕ according to the coordinate transformation

$$x = p\cos\phi - s\sin\phi$$
$$y = p\sin\phi + s\cos\phi \tag{13}$$

where s is the coordinate along the ray direction - see Fig. 8. Next, the object function was differentiated with respect to p and numerically integrated along s, yielding $\lambda'(p,\phi)$.

It was assumed that we have N projections spaced by equal intervals $\Delta\phi = \frac{2\pi}{N}$. The number of data points along the p axis is M thus the increment in p is $\Delta p = \frac{R_0 - R_c}{M-1}$.

2. For each p, $\lambda'(p,\phi)$ is expanded in Fourier Series in the azimuthal direction (Eqs. 3 and 4). The number of terms retained is $\ell_{max} = L$.

3. Equation 8 is used to calculate $f_\ell(r)$, the Fourier coefficients of the azimuthal expansion of the object function. In Eq. 8 the integrand becomes infinite as p->r. The singularity at p=r can be evaluated by dividing the integral in Eq. 8 into two parts[24]

$$-\frac{1}{\pi}\int_r^{R_0} \frac{\frac{d\lambda_\ell(p)}{dp}T_\ell(\frac{p}{r})}{\sqrt{p^2-r^2}}\,dp = -\frac{1}{\pi}\int_r^{r+h} \frac{\frac{d\lambda_\ell(p)}{dp}T_\ell(\frac{p}{r})}{\sqrt{p^2-r^2}}\,dp - \frac{1}{\pi}\int_{r+h}^{R_0} \frac{\frac{d\lambda_\ell(p)}{dp}T_\ell(\frac{p}{r})}{\sqrt{p^2-r^2}}\,dp \tag{14}$$

For small values of h, the first integral is approximated by $-\frac{1}{\pi}[\frac{d\lambda_\ell(r)}{dp}T_\ell(1)\cosh^{-1}(1+\frac{h}{r})]$, thus Eq. 14 becomes

$$-\frac{1}{\pi}\int_{r}^{R}\frac{\frac{d\lambda_{\ell}(p)}{dp}T_{\ell}(\frac{p}{r})}{\sqrt{p^{2}-r^{2}}}\,dp = -\frac{1}{\pi}\{-\frac{d\lambda_{\ell}(r)}{dp}T_{\ell}(1)\cosh^{-1}(1+\frac{h}{r}) + \int_{r+h}^{R}\frac{\frac{d\lambda_{\ell}(p)}{dp}T_{\ell}(\frac{p}{r})}{\sqrt{p^{2}-r^{2}}}\,dp\}$$

(15)

The approximation error is of the order of $O(h^{3/2})$.

4. The object field function is calculated from Eq. 1 using the computed $f_{\ell}(r)$.

A summary of the reconstruction results is given in Table 1.

TABLE 1   Reconstruction Errors Obtained by Inverse Cormack Transform and Iterative Convolution Methods*

Opaque object	N	M	L	Number of grid points	Maximum Error, %	Averaged Error, %
	35	29	8	1015	182.0	9.5
	30	25	6	750	15.8	1.8
Circle ($R_c=0.3R_o$)	30	25	5	750	8.7	1.6
	30	30	5	900	8.5	1.7
	Iterative convolution				19.5	1.8
	35	11	10	385	22.0	2.7
	35	16	6	560	6.5	1.3
	35	16	8	560	5.4	1.3
Circle ($R_c=0.6R_o$)	35	16	10	560	2.0	0.3
	30	16	10	480	5.3	0.6
	30	16	5	480	8.5	1.5
	Iterative convolution				27.5	3.7

*Iterative convolution results are from Ref. 20.

In the table the maximum error is defined as the maximum value of the differences between computed and actual values of the object function at each point, divided by the maximum value of the function that occurs in the object

domain. The average error is defined as the average of the absolute values of the errors over the whole grid. For comparison, the errors calculated by the iterative convolution method are shown in the Table as well. From the Table, it can be seen that for this example, the inverse Cormack transform is considerably more accurate than the iteration method; maximum errors for $R_c = 0.3R_0$ and for $R_c = 0.6R_0$ are 8.5% and 2.0% respectively as compared to errors of 19.5% and 27.5% obtained from the iterative convolutin method, respectively.

IV. CONCLUSIONS

The series expansion approach used in our investigation yielded a fairly efficient reconstruction code. It was shown that the use of the inverse Cormack transform for reconstruction of fields with circular missing deflections data is quite accurate and convenient for use. The accuracy of the algorithm was tested by applying it to data generated by numerical simulation. The relatively high accuracy found is mainly due to the fact that no iterations are necessary.

Our study was limited in this project to asymmetric fields around circular cross sectional opaque objects. It is important to continue and expand the algorithm for elliptical cross-section opaque bodies (which often occur in aeronautics, when circular bodies are at an angle of attack) and for general shaped bodies. Also more analytical studies have to be done in relation to the efficiency of the algorithm.

It has to be emphasized that in the present study we have not made any effort to reduce computational time. The principal factor in determining computational time is the number of grid points and the number of terms retained in the Fourier series. Thus by using the Fast Fourier Transform technique the computational time may be considerably reduced.

APPENDIX

LISTING OF THE COMPUTER RECONSTRUCTION PROGRAM

KF = Number of Fourier coefficients in the series expansion.

NP = Number of data points along p axis.

NFI = Number of projections.

RCRO = R_c/R_o.

DFI = The interval in projection angle.

DP = Increment in p.

MAIN PROGRAM
✻✻✻✻✻✻✻✻✻✻✻✻✻✻✻✻✻✻✻✻✻
THIS PROGRAM RECONSTRUCTS DENSITY FIELDS AROUND CIRCULAR
OPAQE OBJECTS FROM DEFLECTIONS DATA.THIS PROGRAM EMPLOYS
THE INVERSE CORMACK TRANSFORM

```
  IMPLICIT REAL✻8(A-H,O-Z)
  INTEGER IER
  EXTERNAL F,RFF,AIFF,FOU,FOUR
  DIMENSION P(30),FI(60),RDN(60,30),RLMD(30),AILMD(30),RD(60)
  DIMENSION FID(60),RAF(30,60),RIAF(30,60),RREAL(60,30),RAIM(60,3
  DIMENSION XX(60),YY(60),FX(4),FY(4),C(4,3)
  DIMENSION RF(60,30),AIF(60,30)
  COMMON/FM/SP,SN,CS,PM,PCS,PSN
  COMMON/RFM1/RLMD,AILMD,NP
  COMMON/RFM2/P,R,RSQ,IR
  COMMON/AAA/RD,FI,NFIP
  COMMON/BBB/LR,NFI
    DEFINITION OF THE DENSITY FUNCTIONTO BE RECONSTRUCTED
    ✻✻✻✻✻✻✻✻✻✻✻✻✻✻✻✻✻✻✻✻✻✻✻✻✻✻✻✻✻✻✻✻✻✻✻✻✻✻✻✻✻✻✻✻✻✻✻✻✻✻

  PEXP(X,Y)=DEXP(-6.✻((X-0.6)✻✻2+Y✻✻2)/(1.-(X✻X+Y✻Y)))+0.5✻DEXP(-
 #((X+0.6)✻✻2+Y✻✻2)/(1.-(X✻X+Y✻Y)))+DEXP(-6.✻(X✻✻2+(Y-0.6)✻✻2)/(1
 #X✻✻2+Y✻✻2)))+0.5✻DEXP(-6.✻(X✻✻2+(Y+0.6)✻✻2)/(1.-(X✻X+Y✻Y)))

  CALL UERSET(0,LEVOLD)
  PYE=3.14159265358979
  CR=6.0/174.0
  CH=0.01
  AERR=0.
  FAERR=0.
  RO=1.00
  KF=10
```

```
            RCRO=.6
            RERR=.01
            FRERR=0.01
            NP=11
            SRO=RO**2
            RC=RCRO*RO
            NFI=25
            NFIP=NFI+1
            TTL=NFI*NP
            DFI=2.*PYE/NFI
            DFID=360./NFI
            NPM=NP-1
            DP=(RO-RC)/NPM
            DO 10 M=1,NP
            AMM=M-1
            P(M)=RC+DP*AMM
   10    CONTINUE
            DO 11 N=1,NFIP
            AMM=N-1
            FI(N)=DFI*AMM
            FID(N)=DFID*AMM
   11    CONTINUE
            WRITE(6,70) NFI,NP,KF,CH,TTL
   70    FORMAT(2X,'NFI,,NP,,KF,,CH,,TTL',3(3X,I2),3X,2F10.2)

            CALCULATION OF THE DEFLECTION PROJECTIONS (INTEGRAL)
               OF THE GIVEN FUNCTION PEXP(X,Y) FOR THE DEFINED
                  VALUES FI AND P WHICH WE CALL RDN(PHI,P).
            ***********************************************************

            WRITE(6,51)
            DO 12 N=1,NFI
            CS=DCOS(FI(N))
            SN=DSIN(FI(N))
            DO 13 M=1,NPM
            PM=P(M)
            SP=P(M)**2
            PCS=P(M)*CS
            PSN=P(M)*SN
            B=DSQRT(SRO-SP)
            RA=-B
            RDN(N,M)=DCADRE(F,RA,B,AERR,RERR,ERROR,IER)
   13    CONTINUE
            RDN(N,NP)=0.0
   12    CONTINUE
            DO 19 M=1,NP
            RDN(NFIP,M)=RDN(1,M)
   19    CONTINUE
            WRITE(6,50)(FID(N),N=1,NFIP)
            WRITE(6,50)(P(M),M=1,NP)
            DO 53  M=1,NP
            WRITE (6,54) (RDN(N,M),N=1,NFIP)
   53     CONTINUE
   50    FORMAT(3X,10F10.4//)
   54    FORMAT(3X,10F10.4)
   51    FORMAT(3X,'PHI=              P=                    RDN=              ')
```

```
           EXPANSION OF RDN(FI,P) IN FOURIER SERIES
                WITH P ASA PARAMETER
           ***************************************

       SS=0.
       TT=2.*PYE
       DO 17 M=1,NPM
       DO 250 N=1,NFIP
       RD(N)=RDN(N,M)
250    CONTINUE
       DO 26 LR=1,KF
       RREAL(LR,M)=DCADRE(FOU,SS,TT,FAERR,FRERR,ERROR,IER)
       RREAL(LR,M)=RREAL(LR,M)/PYE
       RAIM(LR,M)=DCADRE(FOUR,SS,TT,FAERR,FRERR,ERROR,IER)
       RAIM(LR,M)=RAIM(LR,M)/PYE
26     CONTINUE
17     CONTINUE
       DO 57 LR=1,KF
       RAIM(LR,NP)=0.0
       RREAL(LR,NP)=0.0
57     CONTINUE
       DO 55  M=1,NP
       WRITE(6,56)  M,P(M)
       WRITE(6,54) (RREAL(LR,M),LR=1,KF)
       WRITE(6,54) (RAIM(LR,M),LR=1,KF)
55     CONTINUE
56     FORMAT(4X,'FOURIER COEF. OF RDON ,M=',I3,3X,F6.3)
68     FORMAT(3X,F14.6,2X,F14.6,2X,I4,2X,I4)


        CALCULATION OF THE FOURIER SERIES EXPANSION OF THE
       DENSITY FUNCTION BY USING THE INVERSE CORMACK TRANSFORM
       *************************************************************

       H=CH*RC
       DO 200 IR=1,NPM
       R=P(IR)
       RSQ=R**2
       AR=R+H
       ARH=AR/R
       ACSH=DLOG(ARH+DSQRT(ARH**2-1))
       DO 210 LR=1,KF
       DO 220 M=1,NP
       RLMD(M)=RREAL(LR,M)
       AILMD(M)=RAIM(LR,M)
220    CONTINUE
       RF(LR,IR)=DCADRE(RFF,AR,RO,AERR,RERR,ERROR,IER)
       AIF(LR,IR)=DCADRE(AIFF,AR,RO,AERR,RERR,ERROR,IER)
       RF(LR,IR)=(-1/PYE)*(RLMD(IR)*ACSH+RF(LR,IR))
       AIF(LR,IR)=(-1/PYE)*(AILMD(IR)*ACSH+AIF(LR,IR))
210    CONTINUE
200    CONTINUE


        RECONSTITUTION OFTHE DENSITY FUNCTION FROM THE
        CALCULATED FOURIER COEFFICIENTS
       *********************************************************

       APMR=0.0
       DO 400 IR=1,NPM
       DO 312 N=1,NFI
       RAF(IR,N)=0.5*RF(1,IR)
       RIAF(IR,N)=0.
       DO 300 L=2,KF
```

```
          Z=L-1
          RAF(IR,N)=RAF(IR,N)+RF(L,IR)*DCOS(Z*FI(N))+AIF(L,IR)*DSIN(Z*FI(N))
300       CONTINUE
          X=P(IR)*DCOS(FI(N))
          Y=P(IR)*DSIN(FI(N))
          IF(DABS(1.-X**2-Y**2).LE.CR)   GO TO 444
          PP=PEXP(X,Y)
          GO TO 445
444       PP=0.0
445       CONTINUE
          PPMR=(PP-RAF(IR,N))*100.
          APMR=APMR+DABS(PPMR)
          WRITE(6,18) PP,RAF(IR,N),PPMR,IR,N
 18       FORMAT(3X,F14.6,2X,F14.6,2X,F14.6,2X,I4,2X,I4)
312       CONTINUE
400       CONTINUE
          APMR=APMR/TTL
          WRITE (6,987) APMR,TTL
987       FORMAT(5X///'AVERAGE ERROR=',F10.4,' NUMBER OF POINTS =',F5.1)
          STOP
          END
**********************************************************************
          FUNCTION F(S)
          IMPLICIT REAL*8(A-H,O-Z)
          DIMENSION P(30),RLMD(30),AILMD(30)
          COMMON/RFM1/RLMD,AILMD,NP
          COMMON/RFM2/P,R,RSQ,IR
          COMMON/FM/SP,SN,CS,PM,PCS,PSN
          COMMON/BBB/LR,NFI
          T=SP+S**2
          Q=1.-T
          IF(Q.LE.1.0D-76) GO TO 111
          SQ=Q**2
          SCS=S*CS
          SSN=S*SN
          EF1=(T+0.36-1.2*(PCS-SSN))/Q
          IF(DABS(EF1).GT.29.0)   GO TO 10
          F1=DEXP(-6.0*EF1)
          DF1=-6.0*F1*((2.*PM-1.2*CS)+2.*PM*EF1)/Q
          GO TO 11
10        F1=0.0
          DF1=0.0
11        EF2=(T+0.36+1.2*(PCS-SSN))/Q
          IF(DABS(EF2).GT.29.0)   GO TO 20
          F2=0.5*DEXP(-6.0*EF2)
          DF2=-6.0*F2*((2.*PM+1.2*CS)+2.*PM*EF2)/Q
          GO TO 21
20        F2=0.0
          DF2=0.0
21        EF3=(T+0.36-1.2*(PSN+SCS))/Q
          IF (DABS(EF3).GT.29.0)   GO TO 30
          F3=DEXP(-6.0*EF3)
          DF3=-6.0*F3*((2.*PM-1.2*SN)+2.*PM*EF3)/Q
          GO TO 31
```

```
   30   F3=0.0
        DF3=0.0
   31   EF4=(T+0.36+1.2*(PSN+SCS))/Q
        IF (DABS(EF4).GT.29.0)  GO TO 40
        F4=0.5*DEXP(-6.0*EF4)
        DF4=-6.0*F4*((2.*PM+1.2*SN)+2.*PM*EF4)/Q
        GO TO 41
   40   F4=0.0
        DF4=0.0
   41   CONTINUE
        F=DF1+DF2+DF3+DF4
        GO TO 222
  111   F=0.0
  222   CONTINUE
        RETURN
        END
                     **********************************
        FUNCTION FOU(X)
        IMPLICIT REAL*8(A-H,O-Z)
        DIMENSION FI(60),RD(60)
        COMMON/AAA/RD,FI,NFIP
        COMMON/BBB/LR,NFI
        CALL FINTER(NFIP,FI,RD,X,YY)
        LLL=LR-1
        FOU=YY*DCOS(LLL*X)
        RETURN
        END
                     **********************************
        FUNCTION FOUR(X)
        IMPLICIT REAL*8(A-H,O-Z)
        DIMENSION FI(60),RD(60)
        COMMON/AAA/RD,FI,NFIP
        COMMON/BBB/LR,NFI
        CALL FINTER(NFIP,FI,RD,X,YY)
        LLL=LR-1
        FOUR=YY*DSIN(LLL*X)
        RETURN
        END
                     **********************************
        FUNCTION RFF(X)
        IMPLICIT REAL*8(A-H,O-Z)
        DIMENSION P(30),RLMD(30),AILMD(30)
        COMMON/RFM1/RLMD,AILMD,NP
        COMMON/RFM2/P,R,RSQ,IR
        COMMON/BBB/LR,NFI
        LL=LR-1
        MM=NP
        XR=X/R
        CALL FINTER(MM,P,RLMD,X,YY)
        RFF=YY*DCOSH(LL*DLOG(XR+DSQRT(XR**2-1)))/DSQRT(X**2-RSQ)
        RETURN
        END
```

```
          ******************************
      FUNCTION AIFF(X)
      IMPLICIT REAL*8(A-H,O-Z)
      DIMENSION P(30),RLMD(30),AILMD(30)
      COMMON/RFM1/RLMD,AILMD,NP
      COMMON/RFM2/P,R,RSQ,IR
      COMMON/BBB/LR,NFI
      LL=LR-1
      MM=NP
      XR=X/R
      CALL FINTER(MM,P,AILMD,X,YY)
      AIFF=YY*DCOSH(LL*DLOG(XR+DSQRT(XR**2-1)))/DSQRT(X**2-RSQ)
      RETURN
      END
          ******************************
      SUBROUTINE FINTER(N,XX,YY,X,Y)
      IMPLICIT REAL*8(A-H,O-Z)
      DIMENSION P(30),RLMD(30),AILMD(30)
      DIMENSION FI(60),RDN(60,30)
      COMMON/AAA/RDN,FI
      COMMON/RFM1/RLMD,AILMD,NP
      COMMON/RFM2/P,R,RSQ,IR
      DIMENSION XX(N),YY(N),FX(4),FY(4),C(4,3)
      NF=N
      IF(DABS(XX(1)-X).LE.DABS(1.D-6*XX(1))) X=XX(1)
      IF(DABS(X-XX(NF)).LE.DABS(1.D-6*XX(NF))) X=XX(NF)
      IF(X.LT.XX(1).OR.X.GT.XX(NF)) GO TO 4
      DO 7 I=2,NF
      IF(X.GE.XX(I)) GOTO 7
      K=I-3
      M=2
      IF(I.EQ.2) K=0
      IF(I.EQ.NF) K=NF-4
      IF(I.EQ.2)  M=1
      IF(I.EQ.NF) M=3
      DO 8 J=1,4
      FX(J)=XX(K+J)
 8    FY(J)=YY(K+J)
      CALL IQHSCU(FX,FY,4,C,4,IER)
      Y=((C(M,3)*(X-FX(M))+C(M,2))*(X-FX(M))+C(M,1))*(X-FX(M))+FY(M)
      GOTO 3
 7    CONTINUE
      Y=YY(NF)
      GO TO 3
 4    WRITE(6,5) NF,XX(1),XX(NF),X
 5    FORMAT (1X,'ERROR IN FINTER,X OUT OF RANGE, NF,XX(1),XX(NF),
     # X=',5X,I3,3(3X,D10.3))
 3    RETURN
      END
```

REFERENCES

1. O. Kafri, "Noncoherent Method for Mapping Phase Objects", Opt. Lett. 5, 555 (1980).

2. E. Bar-Ziv, S. Sgulim, O. Kafri and E. Keren, "Temperature Mapping in Flames by Moire Deflectometry", Appl. Opt. 22, 698 (1983).

3. J. Stricker and O. Kafri, "New Method for Density Gradient Measurements in Compressible Flows", AIAA J. 20, 820 (1982).

4. O. Kafri and A. Livnat, "Reflective Surface Analysis Using Moire Deflectometry", Appl. Opt. 20, 3099 (1981).

5. O. Kafri and I. Glatt, "Moire Deflectometry: A Ray Deflection Approach to Optical Testing", Opt. Eng. 24, 944 (1985).

6. E. Keren and O. Kafri, "Diffraction Effects in Moire Deflectometry", J. Opt. Soc. Am. A 2, 111 (1985).

7. E. Bar-Ziv, "Effect of Diffraction on the Moire Image. I. Theory", J. Opt. Soc. Am. A 2, 371 (1985).

8. J. Stricker, "Electronic Heterodyne Readout of Fringes in Moire Deflectometry", Opt. Lett. 10, 247 (1985).

9. J. Stricker, "Diffraction Effects and Special Advantages in Electronic Heterodyne Moire Deflectometry", Appl. Opt. 25, 895 (1986).

10. A.J. Decker and J. Stricker, "A Comparison of Electronic Heterodyne Moire Deflectometry and Electronic Heterodyne Holographic Interferometry for Flow Measurements", SAE Publication No. 851896 14-17 Oct. 1985, Long Beach Convention Center, CA.

11. D.B. Rhodes, J.M. Franke, S.B. Jones and B.D. Leighty, "Moire Deflectometry with Deferred Analysis", Appl. Opt. 22, 652 (1983).

12. J. Stricker and J. Politch, "Holographic Moire Deflectometry - a Method for Stiff Density Fields Analysis", Appl. Phys. Lett. 44, 723 (1984).

13. J. Stricker, "Moire Deflectometry with Deferred Electronic Heterodyne Readout", Appl. Opt. <u>24</u>, 2298, (1985).

14. See for example Technical Information – Agfa–Gevaert, on Photographic Materials for Holography, Aug. 1969. Agfa–Gevaert, Inc. 275 N. Street, Teterboro, N.J. 07608.

15. D. Weimer, "Pockels–Effect Cell for Gas–Flow Simulation", NASA TP–2007 (1982).

16. J. Stricker, "Analysis of 3–D Phase Objects by Moire Deflectometry", Appl. Opt. <u>23</u>, 3657 (1984).

17. S.R. Deans, <u>The Radon Transform and Some of its Applications</u>, (Wiley, New York, 1983).

18. H.H. Barrett and W. Swindell, <u>Radiological Imaging, The Theory of Image Formation, Detection, and Processing</u>, Vol. 2, Chap. 7 (Academic Press, New York, 1981).

19. T.F. Zien and W.C. Ragsdale, "Quantitative Applications of Holographic Interferometry to Wind–Tunnel Testing", Report NOLTR 74-96, Naval Ordance Laboratory, (1974).

20. C.M. Vest and I. Prikryl, "Tomography by Iterative Convolution: Empirical Study and Application to Interferometry", Appl. Opt. <u>23</u>, 2433, (1984).

21. B.P. Medoff, W.R. Brody, M. Nassi and A. Macovski, "Iterative Convolution Backprojection Algorithm for Image Reconstruction from Limited Data", J. Opt. Soc. Am., <u>73</u>, 1493, (1983).

22. J. Stricker, "Mapping of 3–D Density Fields in Flows Around Opaque Objects", Annual Report, Technion Res. and Development Project 161–495 (1986). (Was not published in the literature.)

23. A.M. Cormack, "Representation of a Function by its Line Integrals with Some Radiological Applications", J. App. Phys. 34, 2722 (1963); J. Appl. Phys. 35, 2908 (1964).

24. E. Bar-Ziv, S. Sgulim, O. Kafri and E. Keren, "Temperature Mapping in Flames by Moire Deflectometry", Appl. Opt. 22, 698 (1983).

Fig. 1: Schematics of a conventional moire system. L.S. is a point light source (may be a focused laser beam). M is a parabolic mirror. G_1 and G_2 are Ronchi rulings and S is a mat transparent screen.
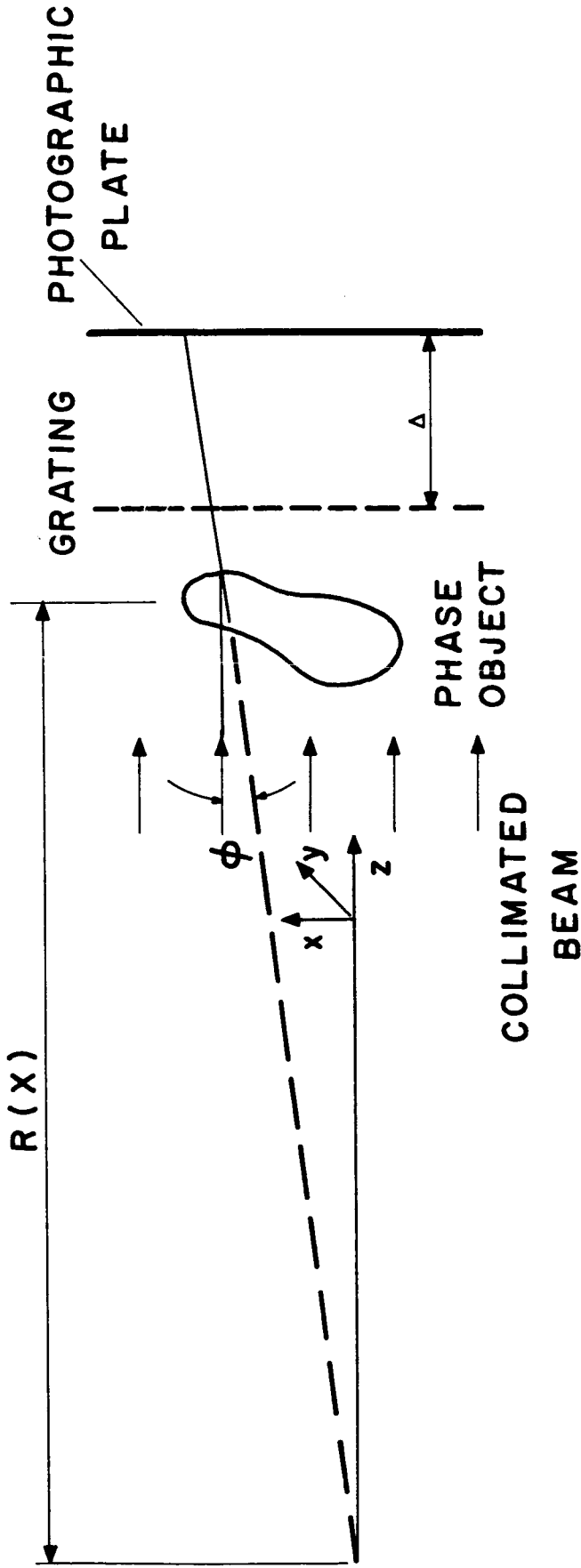
Fig. 2: Schematic of the setup for recording the phase object. ϕ is the refraction angle; $R(x)$ is the distance from the phase object at which the refracted ray seems to emerge.
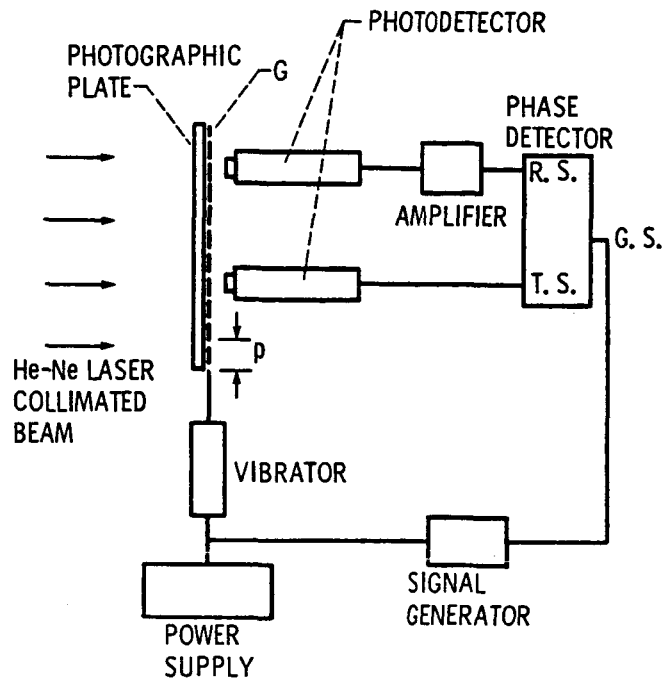
Fig. 3: Schematic of the experimental setup for postanalyzing phase objects:
G, Ronchi ruling; R.S. and T.S., reference and test signals
respectively; G.S., gating signal.
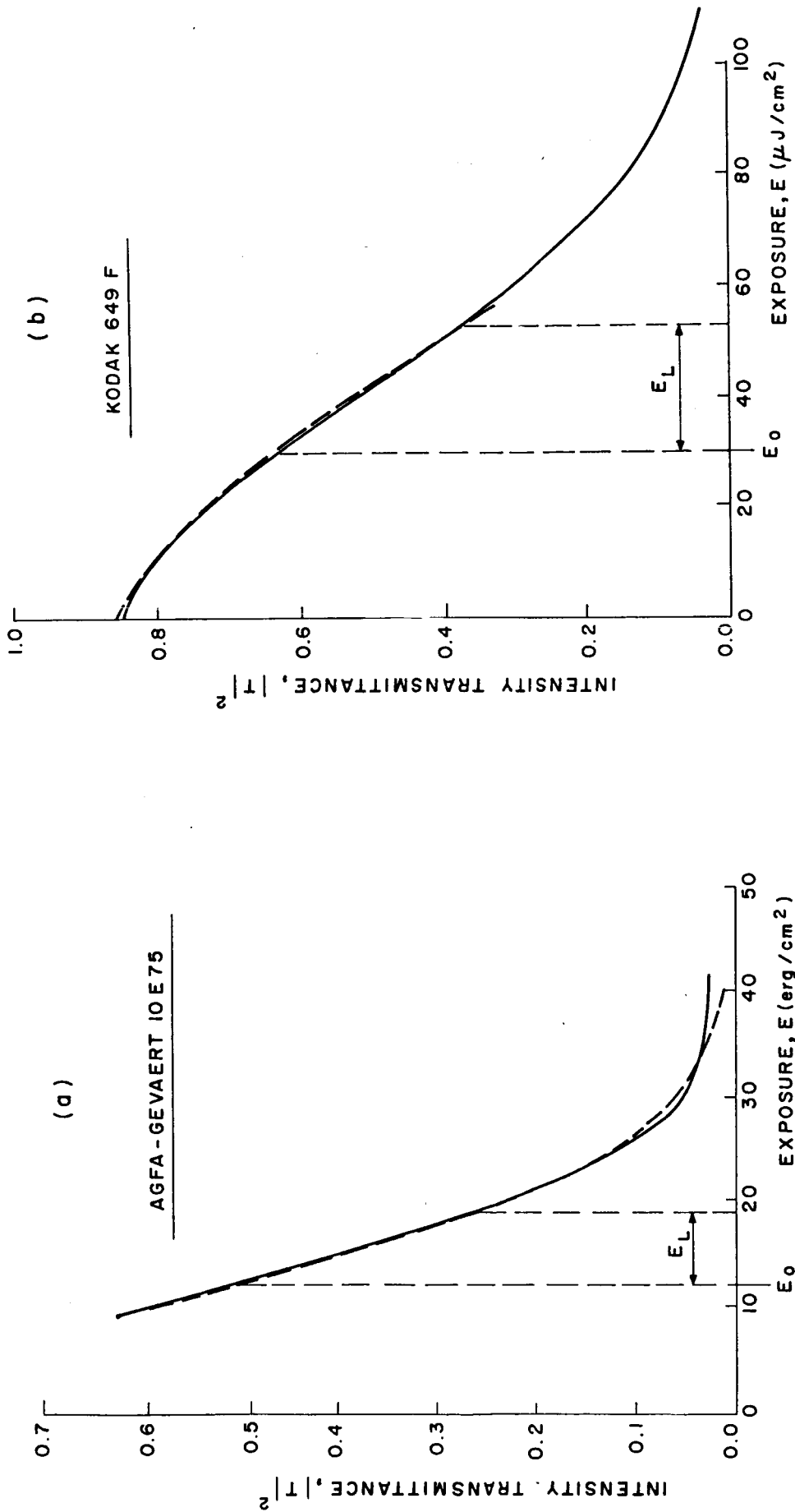
Fig. 4: Intensity transmittance - exposure curves. E_0 and E_L are respectively the width of the linear portion of the curves and the exposure at which they start.
a) Agfa Gevaert 10E75 plate; the dashed curve is the third-order polynomial approximation.
b) Kodak 649F plate; the dashed curve is the second-order polynomial approximation.
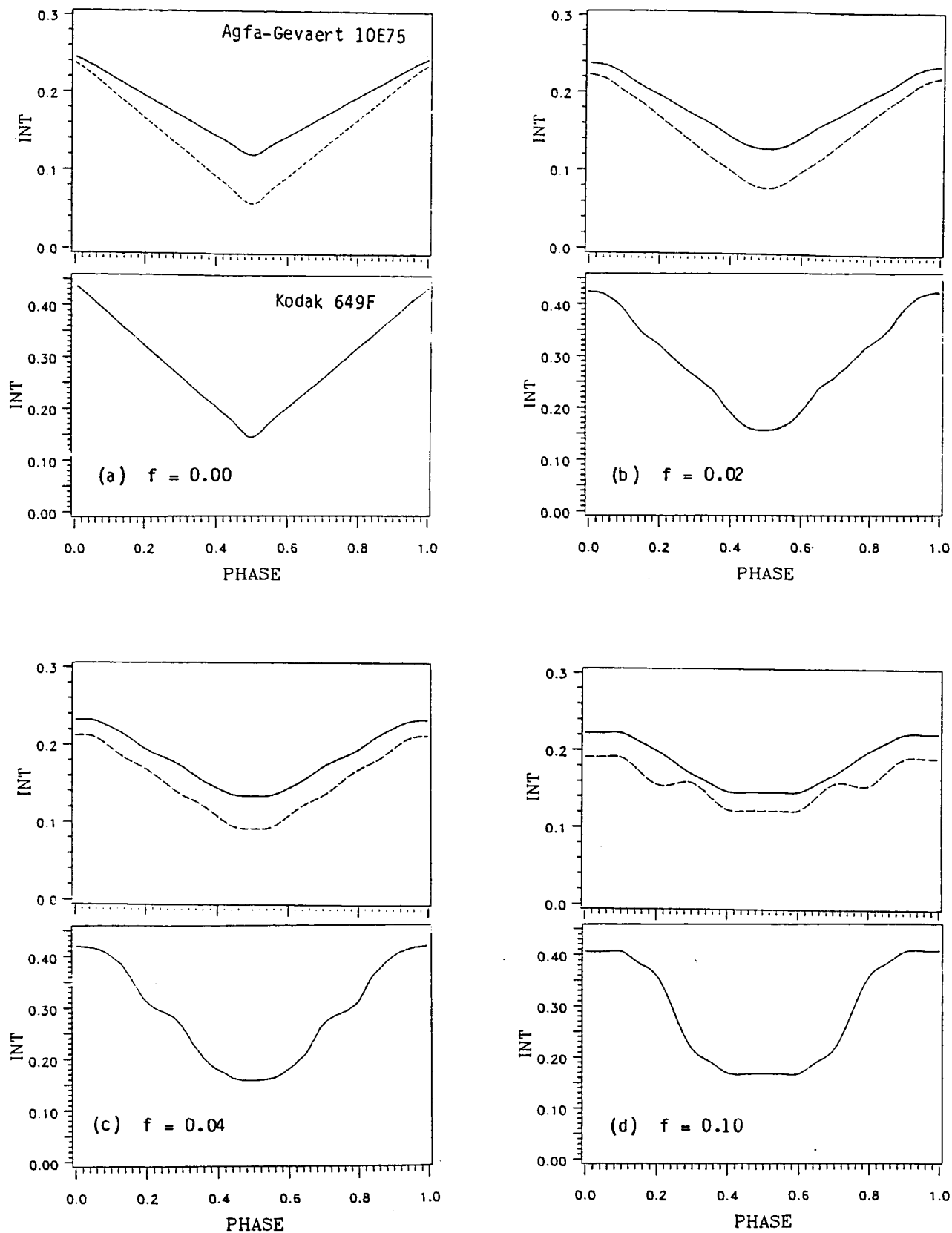
Fig. 5: Calculated moire intensity vs. phase for various values of f. In each figure, the upper two curves are for Agfa-Gevaert 10E75 plates prefogged with exposure $E_0 = 12$ erg/cm^2 and with $E'=8$ erg/cm^2 and $E'=18$ erg/cm^2 for the solid line and dashed line, respectively. The lower curve is for Kodak 649F plates with $E_0=0$ and $E'=55$ μJ/cm^2.
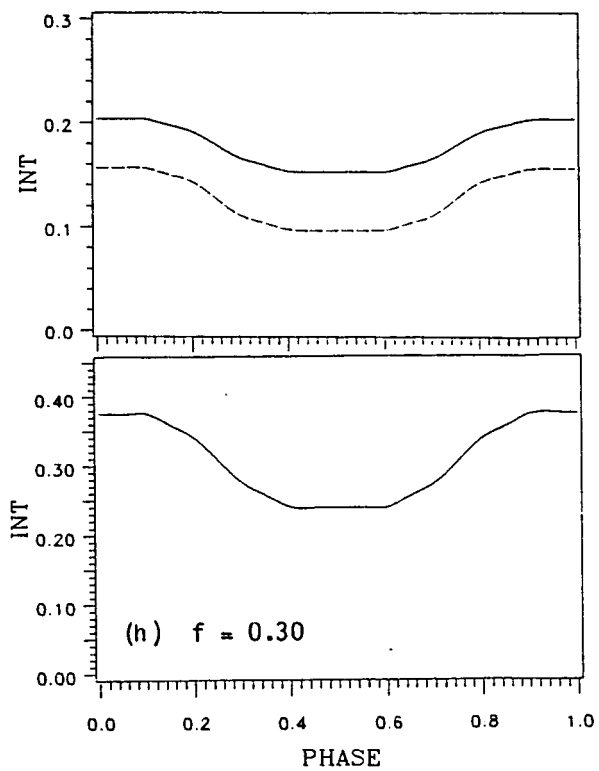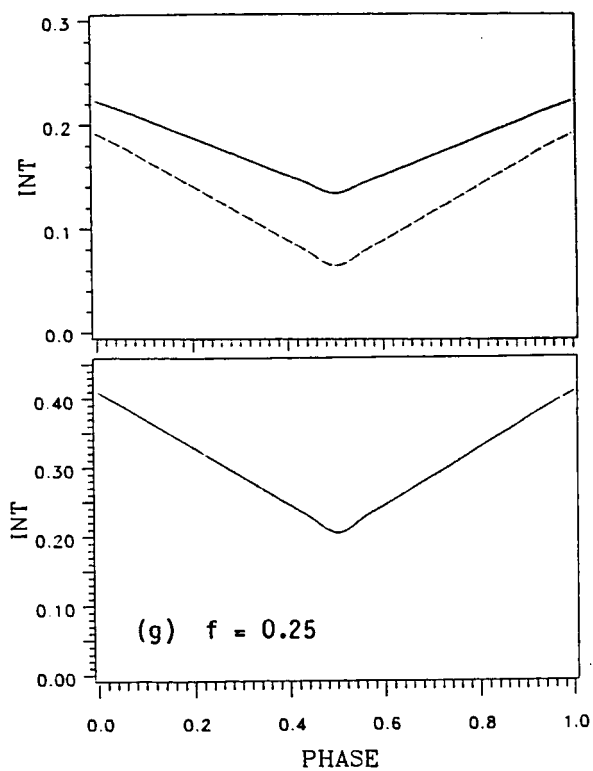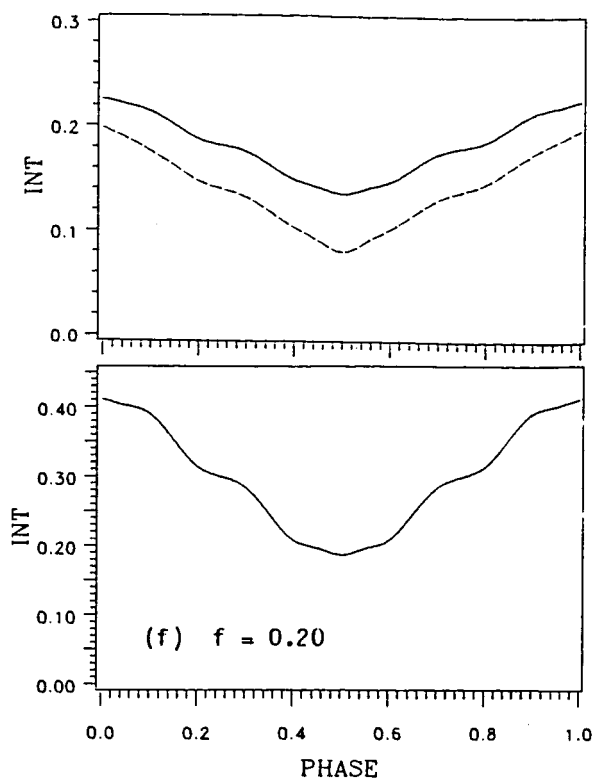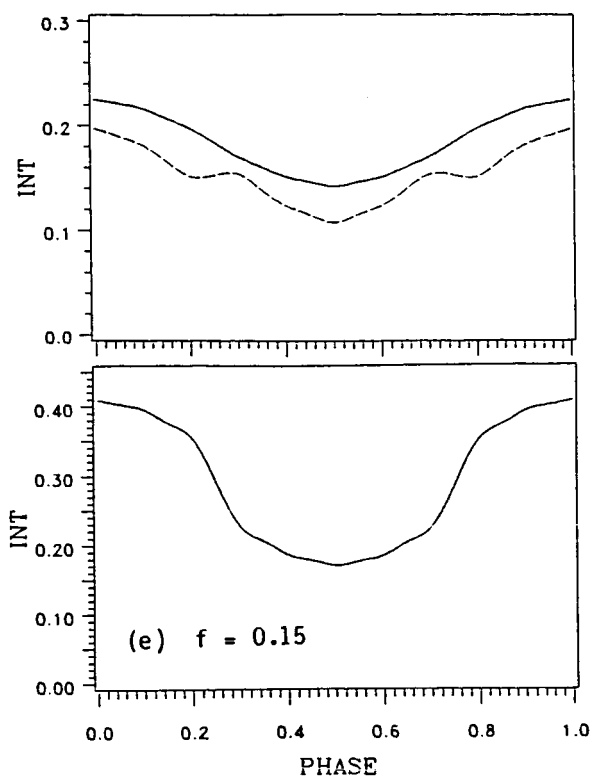
Fig. 5: Calculated moire intensity vs. phase (continued)
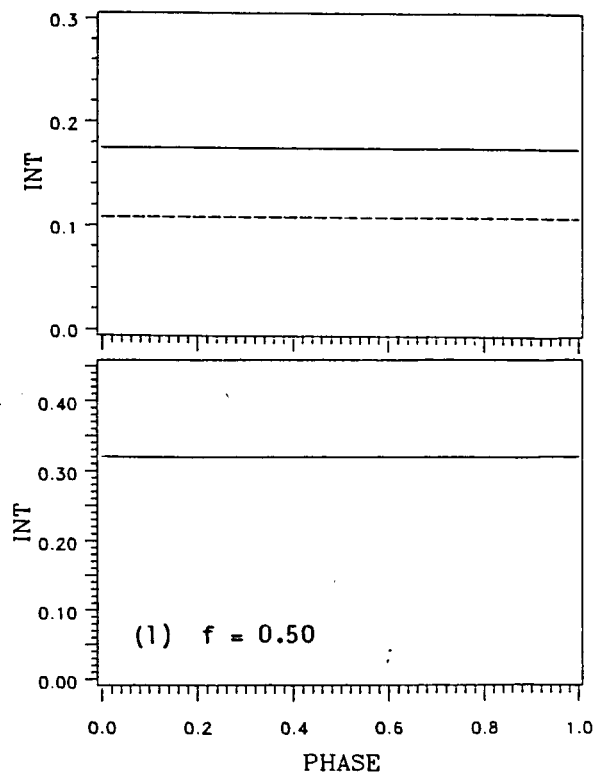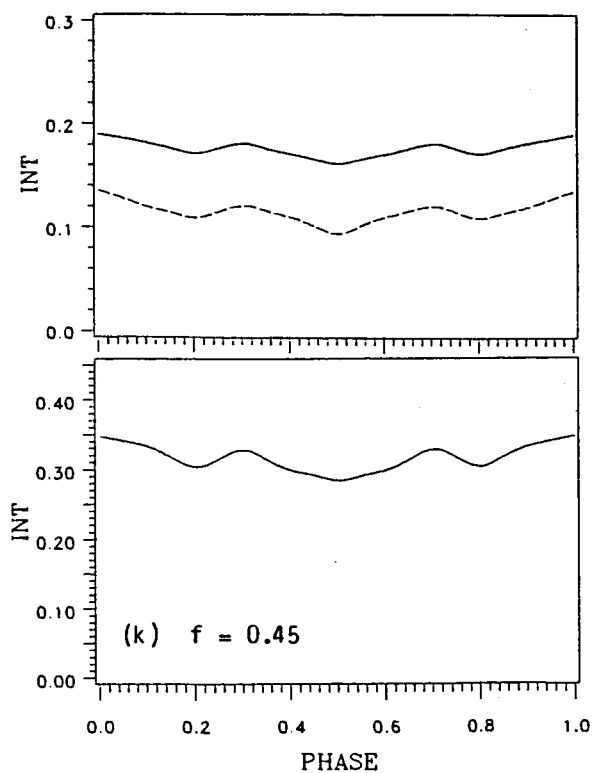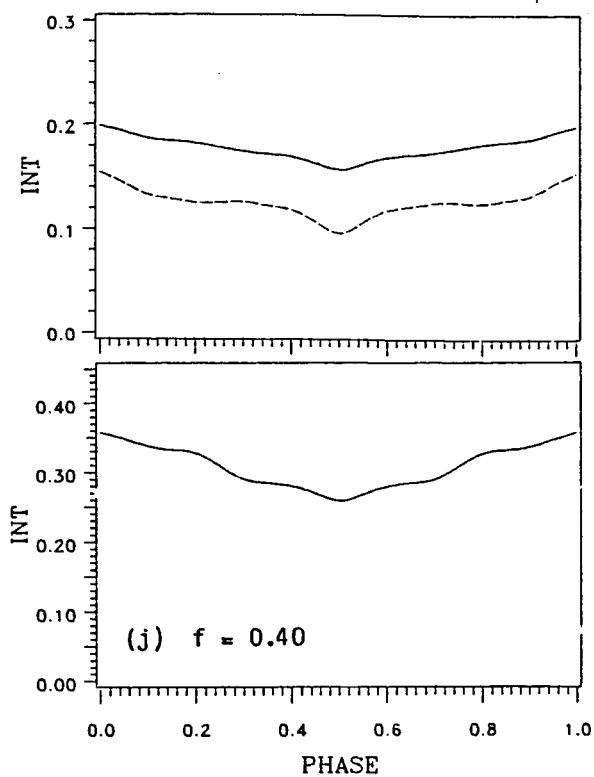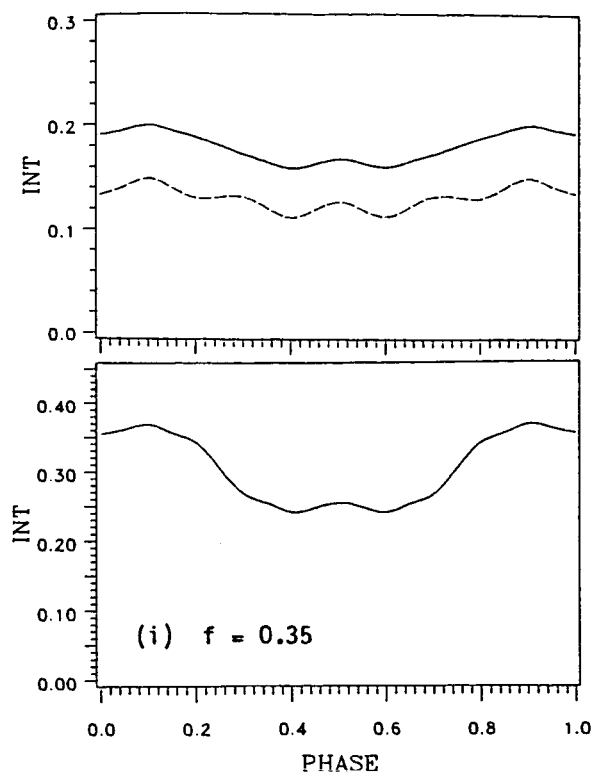
Fig. 5: Calculated moire intensity vs. phase (continued)
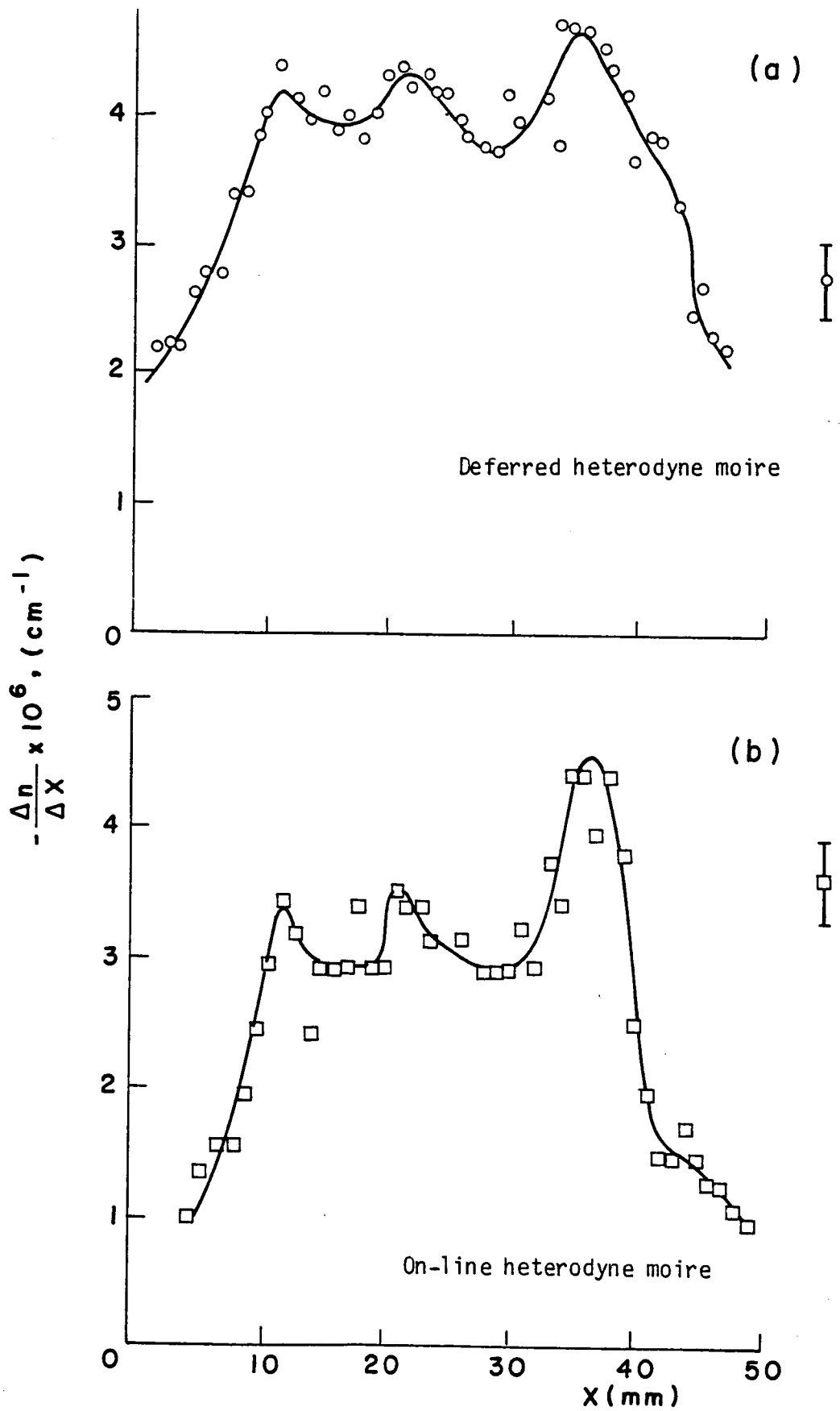
Fig. 6: x - derivative of refraction index for flow simulator.
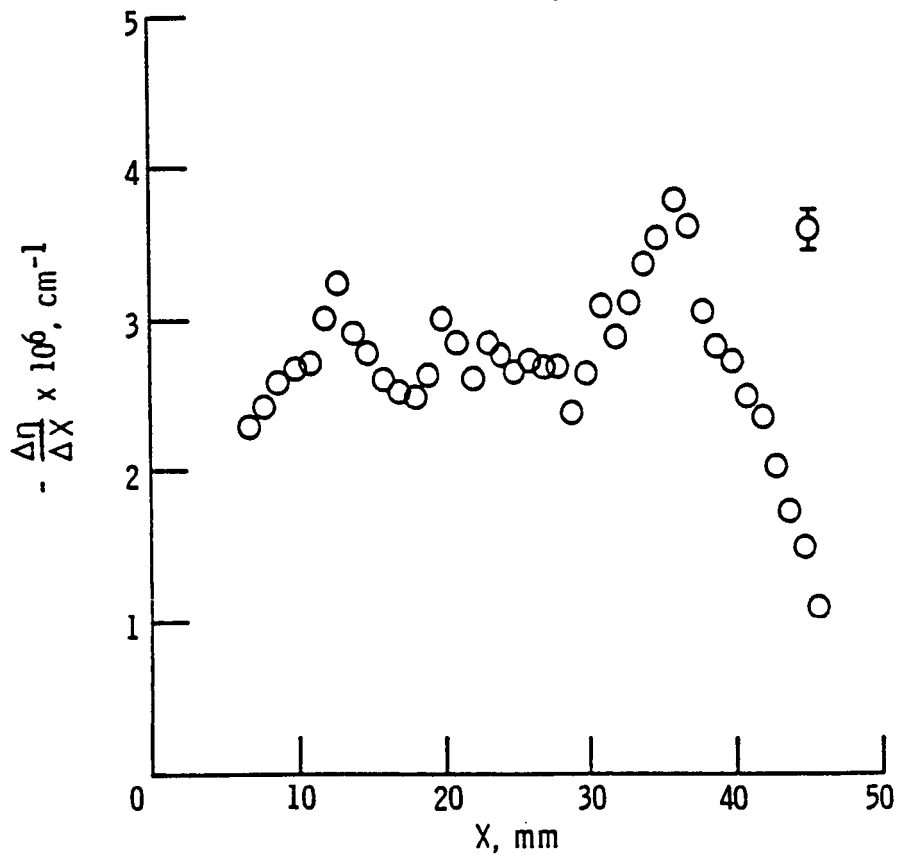
Fig. 7: x - derivative of refraction index for flow simulator - heterodyne holographic interferometry.
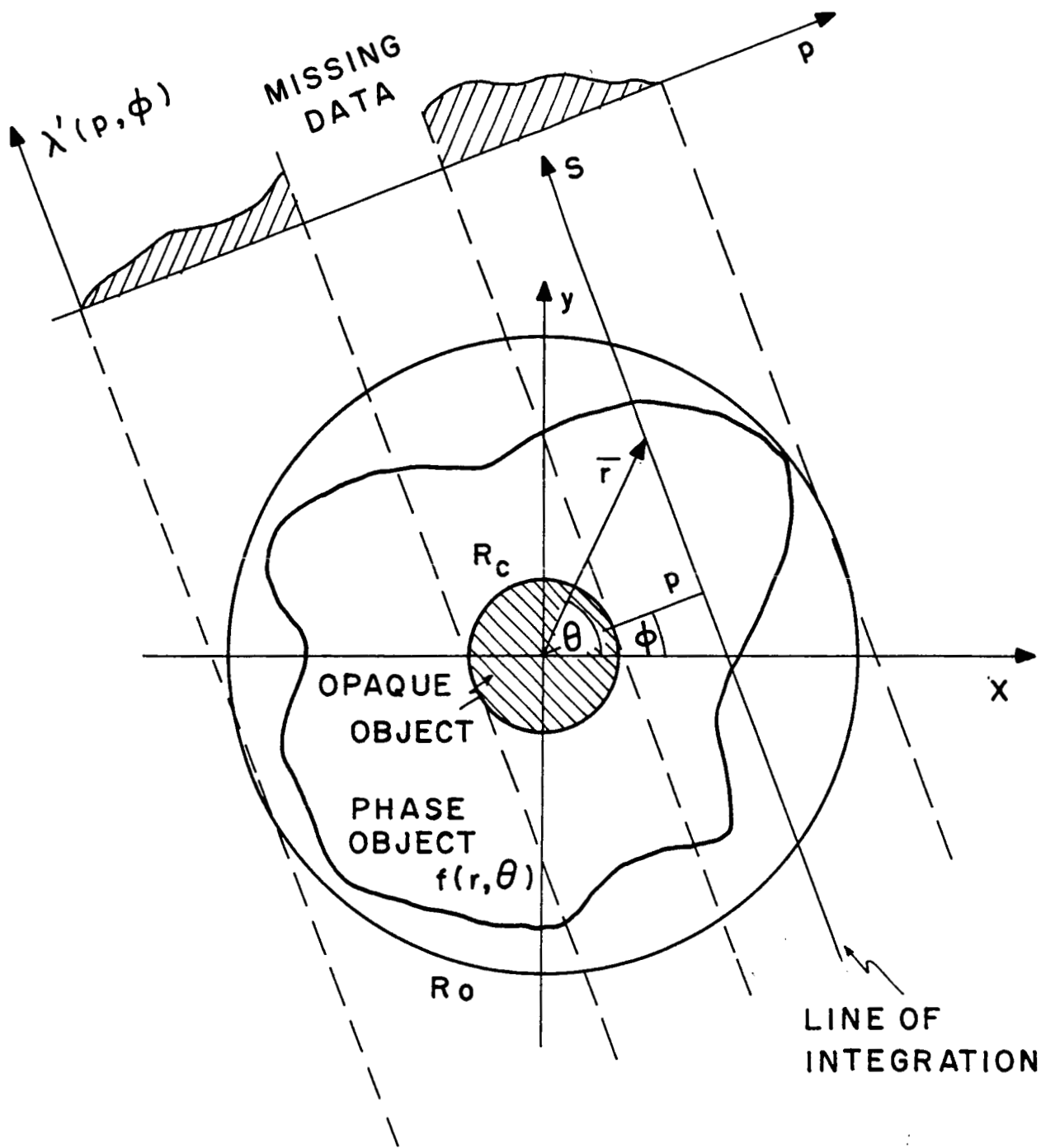
Fig. 8: Object field and the geometry of the transform.
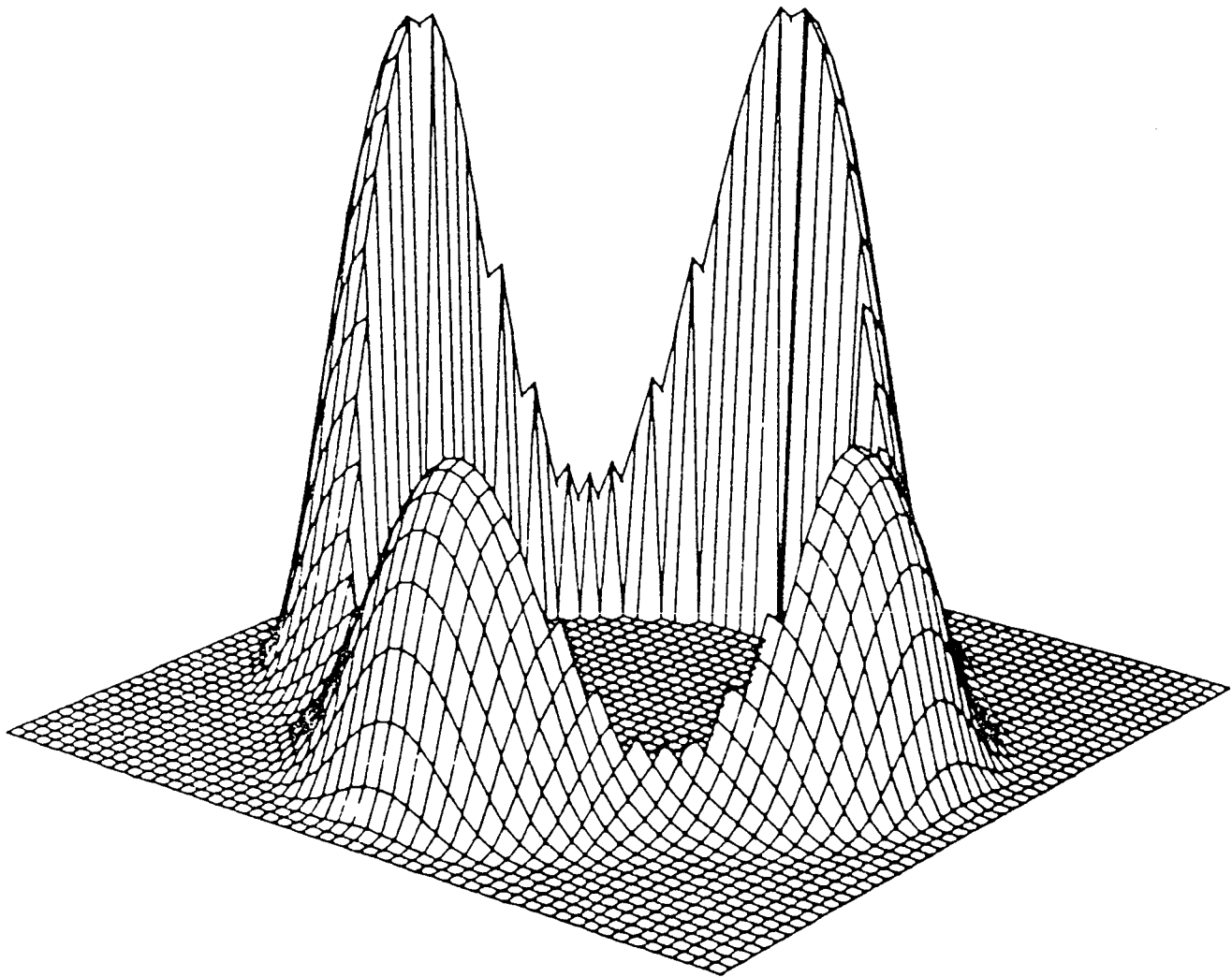
Fig. 9:   The object function used in the study of the algorithm.   The

functions is defined by Eq. 12.   The segment $r < 0.6R_o$ is missing.